In Vitro Polymerization of Microtubules with a Fullerene Derivative

Tatsiana A. Ratnikova,[†,§] Praveen Nedumpully Govindan,[‡,§] Emppu Salonen,[‡,*] and Pu Chun Ke[†,*]

[†]Laboratory of Single-Molecule Biophysics and Polymer Physics, COMSET, Clemson University, Clemson, South Carolina 29631, United States, and [‡]Department of Applied Physics, Aalto University, P.O. Box 11100, FI-00076 Aalto, Finland. [§]These authors contributed equally to the presented work.

ABSTRACT Fullerene derivative $C_{60}(OH)_{20}$ inhibited microtubule polymerization at low micromolar concentrations. The inhibition was mainly attributed to the formation of hydrogen bonding between the nanoparticle and the tubulin heterodimer, the building block of the microtubule, as evidenced by docking and molecular dynamics simulations. Our circular dichroism spectroscopy measurement indicated changes in the tubulin secondary structures, while our guanosine-5′-triphosphate hydrolysis assay showed hindered release of inorganic phosphate by the nanoparticle. Isothermal titration calorimetry revealed that $C_{60}(OH)_{20}$ binds to tubulin at a molar ratio of 9:1 and with a binding constant of $1.3 \pm 0.16 \times 10^6\ M^{-1}$, which was substantiated by the binding site and binding energy analysis using docking and molecular dynamics simulations. Our simulations further suggested that occupancy by the nanoparticles at the longitudinal contacts between tubulin dimers within a protofilament or at the lateral contacts of the M-loop and H5 and H12 helices of neighboring tubulins could also influence the polymerization process. This study offered a new molecular-level insight on how nanoparticles may reshape the assembly of cytoskeletal proteins, a topic of essential importance for illuminating cell response to engineered nanoparticles and for the advancement of nanomedicine.

KEYWORDS: fullerene derivative · tubulin · hydrogen bonding · molecular dynamics simulation · circular dichroism spectroscopy · isothermal titration calorimetry

Recent advancement of nanotechnology in imaging, sensing, and medicine and the mass production of nanomaterials presents a crucial need for fundamental research centered on the behaviors of nanomaterials in biological and ecosystems.[1−4] Fullerenes are a major class of carbon-based nanoparticles that have found applications in materials research, photodynamic therapy, HIV-1 protease inhibition, and facilitated electron transport across a lipid bilayer.[5−8] Once surface functionalized, fullerene derivatives such as $C_{60}(OH)_{20}$ acquire good water solubility while still maintaining their small hydrodynamic diameter.[9] The toxicities of fullerenes and their derivatives have been examined *in vitro*, *in vivo*, and *in silico*, with consistent conclusions yet to be drawn. Notably, Oberdörster reported[10] the accumulation of fullerene C_{60} in the brain of bass and the induced toxicity in the aquatic organism. Sayes *et al.* delineated[11] the differential cytotoxicities of pristine *versus* functionalized fullerenes, which was further corroborated by Qiao *et al.*[12] using atomistic molecular dynamics simulations. Wongekkabut *et al.* illustrated[13] through coarse-grained simulations that fullerenes of high concentrations could induce changes in the structural and elastic properties of the lipid bilayer without causing much mechanical damage, consistent with the observation of cell contraction induced by fullerene C_{70} coated with phenolic gallic acid.[14] Gharbi *et al.* reported[15] that fullerenes were powerful antioxidants with no acute or subacute toxicities in mice. Others[16,17] and our group[18] showed that fullerene derivatives could inhibit polymerase chain reaction (PCR) through their interaction with Taq DNA polymerase. Regarding the ecological fate of carbon nanoparticles, we recently mapped[19] the biodistribution of fullerene C_{70} in rice plants and reported the generational transfer of C_{70} through the plant progeny assisted by natural organic matter (NOM). On the cellular level, we showed[9] the retention of the C_{70}-NOM assembly by the *Allium cepa* plant cell wall and permeation of $C_{60}(OH)_{20}$ through the cell wall to produce a mechanical damage; this trend was reversed for HT-29 mammalian cells, where the amphiphilic C_{70}-NOM assembly induced notable cell damage, while the better suspended $C_{60}(OH)_{20}$ nanoparticles were mostly excluded by the cells.

Despite these ongoing research efforts, it is apparent that little is understood regarding the molecular level interaction between nanoparticles and cell organelles. Microtubules (MTs) are a major component of the cell cytoskeleton and play essential roles in maintaining cell shape, rigidity, motility, vesicle and organelle transport, cell signaling,

* Address correspondence to pcke11@clemson.edu, emppu.salonen@aalto.fi.

Received for review April 11, 2011 and accepted July 15, 2011.

Published online July 15, 2011
10.1021/nn201331n

and cell division in eukaryotes. Under favorable *in vivo* or *in vitro* conditions MTs can be polymerized from tubulin heterodimers of α and β subunits into a cylindrical nanostructure of ~25 nm in diameter and up to micrometers long. Physically MTs can be viewed as polymers possessing a great persistent length and an exceptionally high bending rigidity to suit their versatile bioactivities. Defined by a dynamic instability that is still not well understood, the MT ends can switch abruptly from persistent slow growth to persistent shortening under solution conditions that support assembly.

The assembly of MTs has recently been examined with the introduction of nanoparticles. Specifically, Gheshlaghi *et al.*[20] showed that TiO_2 nanoparticles could alter the MT steady-state equilibrium and change tryptophan positions in tubulins to move them toward GTP binding sites. Apopa *et al.* found[21] that iron nanoparticle-induced reactive oxygen species (ROS) production could regulate cell permeability through remodeling of MTs in human microvascular endothelial cells. Using surface-enhanced Raman spectroscopy, Zhou *et al.* identified[22] a variety of tubulin functional groups including imidazole, sulfur, aromatic rings, amine, and carboxylate, which interacted with gold nanoparticles, with the imidazole ring in the histidine acting as the most prominent functional group for the binding.

In view of the ubiquitous structural and functional roles of cytoplasmic proteins and the prevalent synthesis of carbon nanoparticles in research laboratories and by the industry, this paper examines the *in vitro* polymerization of MTs in the presence of $C_{60}(OH)_{20}$. Specifically, in the following sections we present our study based on the methodologies of fluorescence imaging, circular dichroism (CD) spectroscopy, isothermal titration calorimetry (ITC), guanosine-5′-triphosphate (GTP) hydrolysis, and docking and atomistic molecular dynamics computer simulations. Our results indicate that $C_{60}(OH)_{20}$ inhibits MT assembly *via* the formation of multiple hydrogen bonds between the nanoparticle and its neighboring tublin subunit. The binding between $C_{60}(OH)_{20}$ and the nucleotides, both exchangeable during GTP hydrolysis and immutable in α units, is another possible cause for the changes in the tubulin secondary structures and inhibited MT polymerization.

RESULTS AND DISCUSSION

Inhibition of Tubulin Polymerization by $C_{60}(OH)_{20}$. As the concentration of $C_{60}(OH)_{20}$ was increased from 1 to 30 mg/L, the average length of polymerized MTs was shortened accordingly (Figure 1). Both bimodal and normal single-peak distributions were shifted to the left with the addition of the nanoparticles, indicating inhibition of MT polymerization. Specifically, the presence of the highest $C_{60}(OH)_{20}$ concentration of 30 mg/L led to the shift of the single-peak distribution to be centered at 3 μm, indicating that most of the polymerized MTs were shorter than the ones for the control, where two distribution peaks were observed at 5 and 20 μm. Also, we observed that the quantity of polymerized MTs per field of view was reduced under the fluorescence microscope with the addition of $C_{60}(OH)_{20}$, and smaller broken segments of MTs were frequently observed (Figure 1B). To quantify this phenomenon, we further counted the number of polymerized MTs on each coverglass substrate, and the average number of polymerized MTs was obtained for 20 slides of each sample condition. The MTs shorter than 1 μm or with a curvature/bending of more than 30° were not taken into consideration to eliminate error introduced by the instrument resolution and diffraction limit. As shown in Figure 2, the amount of polymerized MTs was significantly reduced with $C_{60}(OH)_{20}$ concentrations at or above 5 mg/L. Specifically, the presence of the highest $C_{60}(OH)_{20}$ concentration of 30 mg/L led to a 50% decrease in the number of polymerized MTs.

Three interactions could have contributed to the hindered MT polymerization. One is that the hydroxyl groups of the nanoparticles could form hydrogen bonding with the electronegative elements on the tubulin surfaces, similar to that described for the interaction between free dNTPs and $C_{60}(OH)_{20}$ in the PCR process;[18] the other is the electrostatic interaction between the negatively charged $C_{60}(OH)_{20}$ in the reaction buffer—according to the zeta potential measurement—with the abundant amine groups on the protein surfaces. However, since the two carboxyl termini of each tubulin carry a significant electric charge, electrostatic binding between $C_{60}(OH)_{20}$ and assembled MTs is unlikely due to their mutual repulsion, although short-range hydrogen bonding between the nanoparticles and the GDP in the MT protofilaments could still take place to facilitate their close contact. Furthermore, due to the steric hindrance of the hydroxyl moieties of the nanoparticles, π-stacking between the sp^2 electrons in the $C_{60}(OH)_{20}$ and the aromatic groups on the tubulin surfaces is not expected to be a contributing factor. In addition to the above two interactions, a third plausible cause for the hindered MT polymerization is that $C_{60}(OH)_{20}$ could be involved in the biochemical process of GTP hydrolysis, through either forming hydrogen bonds with the free nucleotides in the reaction or altering the length and structure of the GTP cap at the growing ends of the MT to impact the polymerization; in either case the conformational changes in the tubulins or in the nucleotides could disrupt the vertical assembly of the tubulins into protofilament or the lateral weak bonds between the tubulins into a sheet that is subsequently curled into a tube.

$C_{60}(OH)_{20}$ Binding Induced Secondary Structural Changes in Tubulin. To delineate the binding mechanisms for tubulin and $C_{60}(OH)_{20}$, CD spectra of the protein were acquired at room temperature. As illustrated in Figure 3,

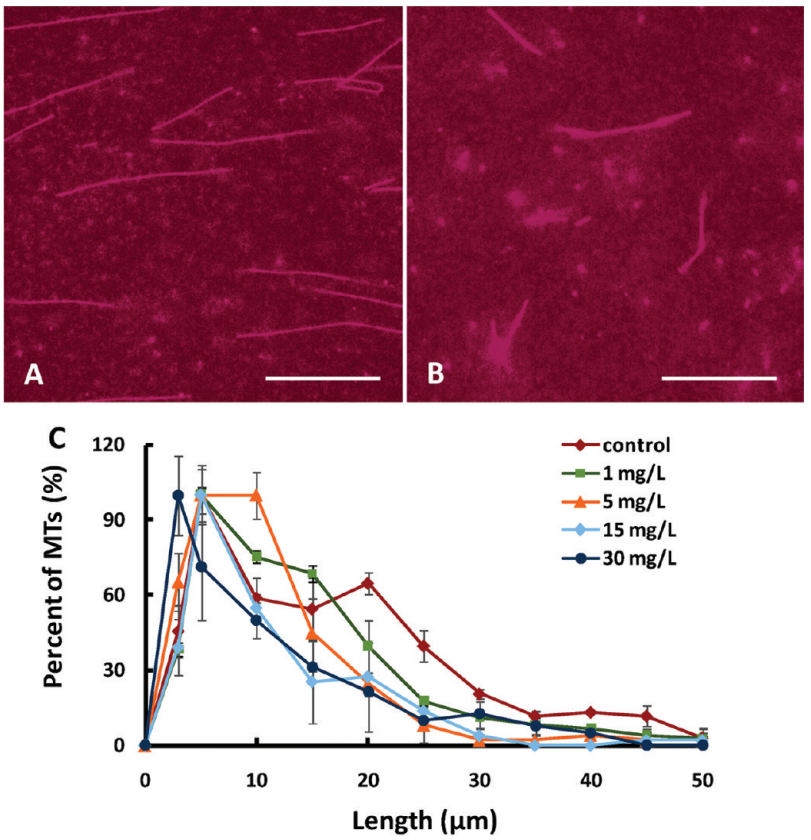

Figure 1. (A) Control polymerization of MTs. (B) MT polymerization in the presence of $C_{60}(OH)_{20}$ of 15 mg/L. Scale bars: 20 μm. (C) Length distribution of polymerized MTs (normalized by peak values) *vs* $C_{60}(OH)_{20}$ concentration. Approximately 200 MTs were analyzed for each sample condition.

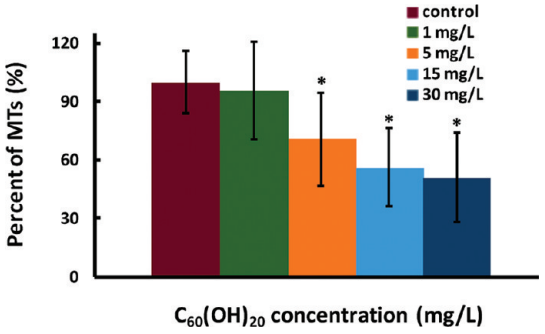

Figure 2. Number of polymerized MTs (normalized by the control) *vs* $C_{60}(OH)_{20}$ concentration. Statistically significant differences between the samples and the control were determined by the Student *t* test (*$p < 0.05$).

addition of the nanoparticles to the reaction altered the far-UV circular dichroism spectrum of the tubulin, indicating that $C_{60}(OH)_{20}$ indeed bound to the protein to induce a conformational change in the latter. The mathematical method SELCON[24,25] was used to calculate percents of the secondary structures of the protein, based on the linear dependence between structural fractions and the spectra (see Figure 3). As $C_{60}(OH)_{20}$ concentration increased, more α helices were turned into β sheets or denatured further into linear structures since the total percent of α and β sheets was decreased by 6.9% when $C_{60}(OH)_{20}$ concentration was increased

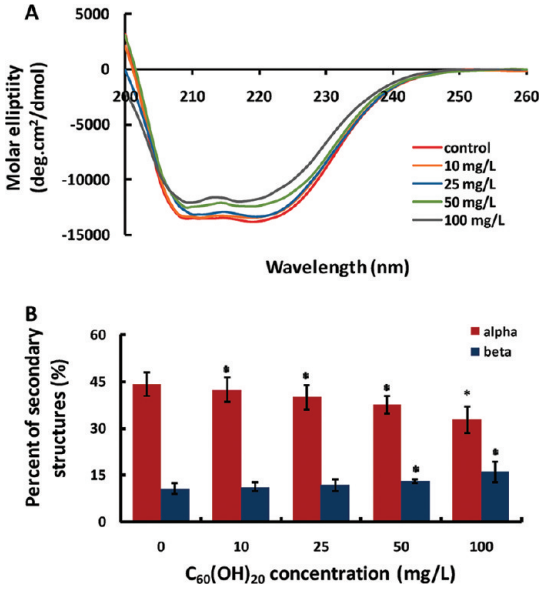

Figure 3. (A) Circular dichroism spectra in the presence of $C_{60}(OH)_{20}$. (B) Percent of secondary tubulin structures *vs* $C_{60}(OH)_{20}$ concentration. Statistically significant differences between the samples and the control (0 mg/L) were determined by the Student *t* test (*$p < 0.05$).

from zero to 100 mg/L. The CD spectra of pure proteins incubated under the same conditions were acquired, which showed no significant changes in their secondary

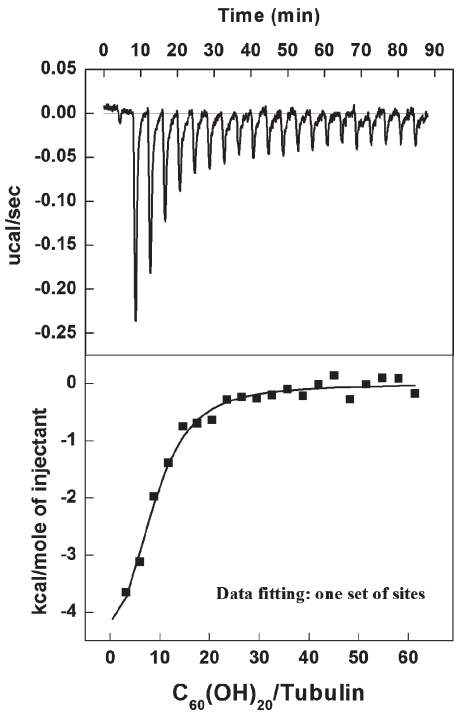

Figure 4. Calorimetric titration of tubulins with $C_{60}(OH)_{20}$ at 25 °C. The upper panel shows raw data, obtained from 22 injections (14 μL each) of $C_{60}(OH)_{20}$. The lower panel shows the plot of total energy exchanged (as kcal/mol of injectant) as a function of the molar ratio of $C_{60}(OH)_{20}$ to tubulin. The theoretical curve fitted to the intergraded data yields $\Delta G = -6.343$ kcal/mol and $\Delta H = -2.648$ kcal/mol. On average nine $C_{60}(OH)_{20}$ moleules were bound to one tubulin monomer, and the binding constant K was determined as $(1.3 \pm 0.16) \times 10^6$ M^{-1}.

structures. This step confirmed that changes in the secondary structures of the tubulin were induced by the binding of the nanoparticle, not by protein denaturation, through the first or second mechanism previously described.

ITC of Tubulin−$C_{60}(OH)_{20}$ Binding. The inhibition of microtubule polymerization can be attributed to the binding of $C_{60}(OH)_{20}$ with tubulin. Figure 4 shows a serial titration analysis of the interaction of $C_{60}(OH)_{20}$ and tubulin. Since ITC measurements require high protein concentrations, the measured parameters are independent of the state of the tubulin. The titration consisted of addition of small aliquots of $C_{60}(OH)_{20}$ per shot per 4 min interval to 0.7 μM tubulin in PEM buffer without GTP at 298 K. The titration showed monotonic decrease in the exothermic heat of binding with successive injections until saturation. The upper panel of Figure 4 displays raw data in power *versus* time prior to baseline subtraction. The area under each injection peak is proportional to the heat produced. The lower panel of Figure 4 displays the binding isotherm created by plotting the integrated peaks against the molar ratio of $C_{60}(OH)_{20}$ added to the tubulin. The heat of diluting $C_{60}(OH)_{20}$ in the buffer was taken into account for calculating the thermodynamic parameters. The theoretical curve fitted to the intergraded data yields $\Delta G = -6.343$ kcal/mol and $\Delta H = -2.648$ kcal/mol. On average nine $C_{60}(OH)_{20}$ moleules were bound to one tubulin monomer, and the binding constant K was determined as $(1.3 \pm 0.16) \times 10^6$ M^{-1}.

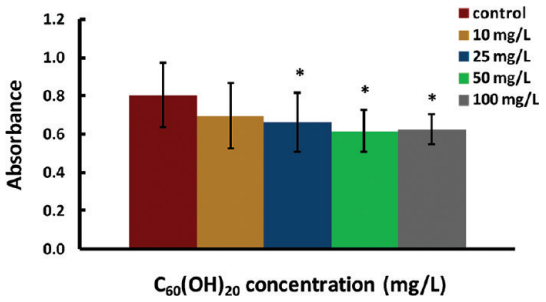

Figure 5. GTP hydrolysis (phosphate release) *vs* $C_{60}(OH)_{20}$ concentration. Statistically significant differences between the samples and the control were determined by the Student *t* test (*$p < 0.05$).

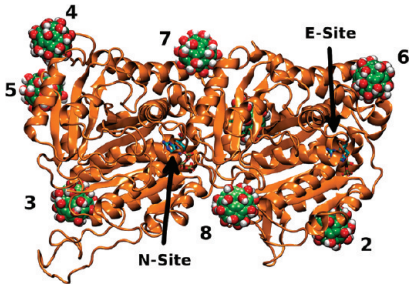

Figure 6. Eight binding sites of $C_{60}(OH)_{20}$ on tubulin dimer (α subunit on the left side and β subunit on the right side) identified from docking simulations. The GTP/GDP binding E-site in the β subunit and the N-site in the α subunit are indicated by arrows and highlighted in blue. No binding was observed near the E-site.

Effect of $C_{60}(OH)_{20}$ on GTP Hydrolysis. Tubulin is a GTPase that hydrolyzes its bound nucleotide triphosphate.[39] During MT polymerization, both the α and β subunits of a tubulin dimer are bound to a GTP molecule, and the tubule elongates from the minus end to the plus end. While the GTP bound to α tubulin is stable, the GTP bound to β tubulin may be hydrolyzed by the protein to GDP and an inorganic phosphate shortly after assembly. A GDP-bound tubulin subunit is prone to depolymerization and will fall off at the tip of an MT or remain integrated if it resides in the middle of the tubule.[39] Once a GTP-bound tubulin is added to the tip of the MT, a new cap is formed to stimulate the growth of the tubule. When hydrolysis catches up to the plus end of the MT, polymerization is switched to shrinkage through the process of catastrophe.[40]

As shown in Figure 5, the release of inorganic phosphate during GTP hydrolysis was impaired by the presence of $C_{60}(OH)_{20}$ at concentrations of 25 mg/L and above. Interestingly, such inhibition did not increase much for higher nanoparticle concentrations of 50 and 100 mg/L, by ~5% respectively in comparison with the control. The reduced release of phosphate during MT polymerization is a direct indication of the

TABLE 1. Eight Most Important Binding Sites and Their Properties Predicted by Docking Simulations

site	lowest binding energy (kcal/mol)	population	residues[a] within 0.7 nm of $C_{60}(OH)_{20}$
1	−6.45	85	Asn 102, Glu 411, His 406, *Arg 158, Asp 163, Asn 197, Thr 198, Asp 199, Val 257, Phe 262, Arg 264, His 266*
2	−4.05	60	*Pro 89, Asp 90, Asn 91, Phe 92, Val 93, Phe 94, Leu 114, Ser 117, Asp 120, Val 121, Lys 124, Arg 79*
3	−4.03	91	Phe 49, Asn 50, Phe 53, Arg 123, Asp 127, Cys 129, Leu 130, Phe 135, Tyr 161, Lys 163, Lys 164
4	−3.72	57	Lys 336, Thr 337, Lys 338, Arg 339, Thr 340, Gln 342, Phe 343, Asp 345
5	−3.34	97	Thr 257, Asn 258, Val 260, Pro 261, Tyr 262, Trp 346, Cys 347, Pro 348, Thr 349
6	−2.65	86	*Val 177, Ser 178, Thr 180, Val 181, Val 182, Glu 183, Pro 184, Tyr 185, Arg 390, Glu 393, Gln 394, Phe 395, Phe 404, Lys 176*
7	−3.97	33	Gln 176, Arg 390, His 393, Lys 394, Leu 397, *Leu 333, Gln 336, Asn 337, Glu 345, Trp 346, Ile 347, Pro 348, Asn 349, Asn 350*
8	−2.99	45	*Tyr 36, Asp 39, Ser 40 Asp 41, Leu 42, Gln 43, Ile 358, Pro 359, Arg 369*

[a] Alpha subuint residues in normal and β subunit residues in italic typeface.

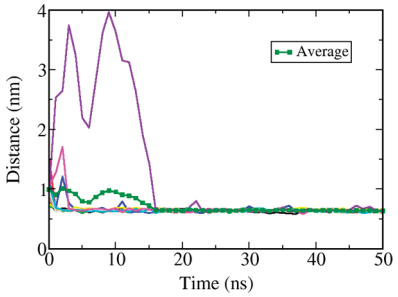

Figure 7. Minimum distances between 10 $C_{60}(OH)_{20}$ molecules and tubulin in a simulation and their average.

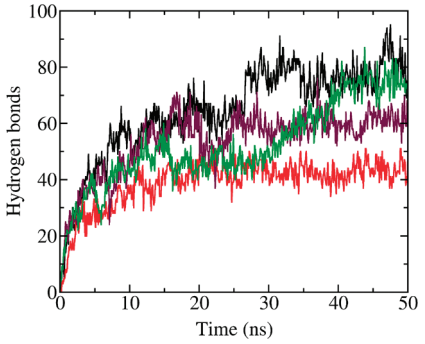

Figure 8. Number of hydrogen bonds between 10 $C_{60}(OH)_{20}$ molecules and tubulin in four independent simulations.

shrinkage of the GTP cap length at the growing ends of the MT, which would give rise to increased instability in the MT architecture.

Binding by Docking and MD Simulations. The 1000 conformations from docking were analyzed to identify the most important binding sites of $C_{60}(OH)_{20}$ on tubulin dimer. The conformations were grouped into different clusters based on root-mean-square deviations (rmsd's) of their coordinates. Conformations with their mutual RMSDs within 0.8 nm were considered to be in the same cluster. Different conformations in the same cluster thus represent different binding modes at the same binding site. Eight binding sites were identified as the most important ones based on the binding energy, population of the cluster, and relevence of the site for polymerization (Figure 6). Table 1 summarizes the binding energies and molecular populations of these eight sites. The obtained binding energies range between −6.45 and −2.99 kcal/mol for the eight most prominent sites. These values are in a reasonable agreement with the ITC data analysis based on the single-site binding model (−6.34 kcal/mol, see above).

The MD simulations started with 10 $C_{60}(OH)_{20}$ molecules positioned randomly around the tubulin dimer. In all the simulations, it was observed that $C_{60}(OH)_{20}$ binds to different locations around the protein. That is, as in the docking simulations, a single predominant binding site seems to be absent. Instead, $C_{60}(OH)_{20}$ prefers sites with many charged or polar residues. Both of these are consistent with the ITC measurements, which showed that up to nine $C_{60}(OH)_{20}$ molecules bound to each tubulin dimer.

Once anchored at these binding sites, $C_{60}(OH)_{20}$ remained bound throughout the simulations. This is illustrated in the plot of minimum distances between 10 $C_{60}(OH)_{20}$ molecules and one tubulin (Figure 7). Upon binding to the tubulin, $C_{60}(OH)_{20}$ molecules form a number of hydrogen bonds with charged or polar residues. Figure 8 shows the number of hydrogen bonds as a function of time for four simulations. On average, each $C_{60}(OH)_{20}$ molecule forms approximately six hydrogen bonds with the tubulin.

It was observed in our experiment that the total percent of α helices and β sheets was decreased by 6.9% as $C_{60}(OH)_{20}$ concentration was increased from zero to 100 mg/L (Figure 3). To check this, the secondary structure of tubulin was analyzed for two, *set I* and *set II*, simulations (sets without and with $C_{60}(OH)_{20}$ molecules, respectively) using the secondary structure assignment algorithm DSSP.[41] First, there was an overall tendency (for both sets) for a decrease in the number of α helix residues and increase in β sheet residues due to the inherent nature of the Gromos force field.[42] The number of residues forming β sheets was slightly larger [(1.9 ± 1.7)%] in *set II* simulations compared to *set I* simulations. Similarly, the number of α helix residues was slightly smaller [(1.8 ± 1.1)%] in *set II* simulations compared to *set I* simulations. Although these observations are consistent with the experimental results,

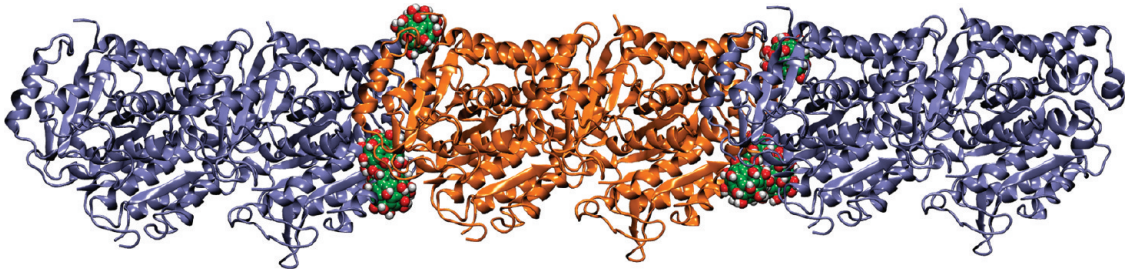

Figure 9. Contact between a tubulin dimer (orange) and its longitudinal neighbors (blue) in a protofilament. All the $C_{60}(OH)_{20}$ binding sites at the two longitudinal interfaces predicted by MD are shown.

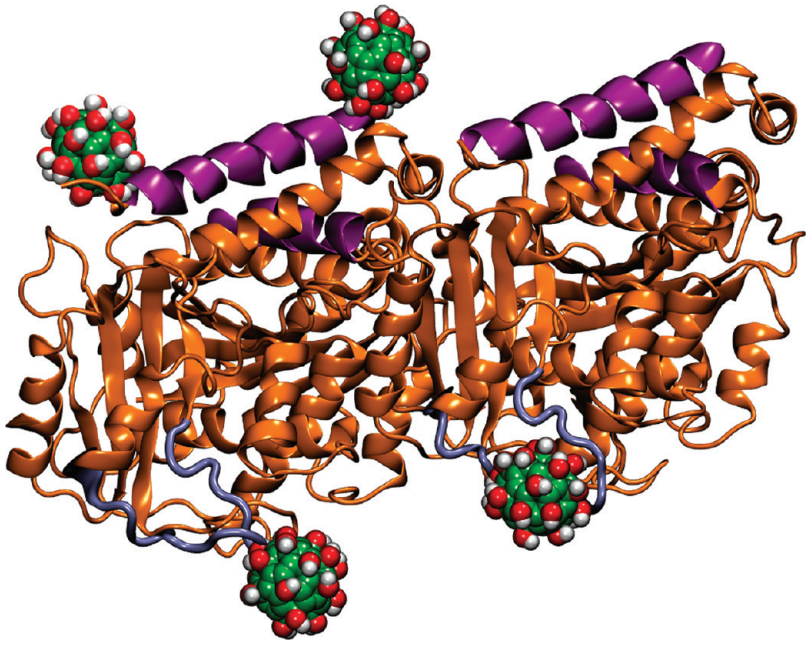

Figure 10. Interaction between the M-loop of one dimer (blue) and the helices H5 and H12 (purple) in a neighboring dimer contribute most to the interdimer lateral contacts in zinc sheets. $C_{60}(OH)_{20}$ was observed to make contacts with these structures in MD simulations.

the differences are very small. Futher, between the two sets, there was no noticeable difference in the total number of residues forming α helix or β sheets.

The binding of $C_{60}(OH)_{20}$ to tubulin-bound GTP/GDP can affect the GTP hydrolysis or GDP/GTP exchange and thus MT dynamics. It has been shown that $C_{60}(OH)_{20}$ can bind to the triphosphate tail of dNTP, with a binding energy greater than 10 kJ/mol.[18] Since dNTPs and nucleoside triphosphates (NTPs) share the same structures, except that the 2′ hydroxyl group is replaced by a hydrogen atom in the former, $C_{60}(OH)_{20}$ should bind to GTP with a similar binding energy. However, $C_{60}(OH)_{20}$ was not found to bind to tubulin-bound GTP/GDP in either MD or docking studies. This is probably due to the size and shape of the GTP/GDP binding site of the tubulin, which is not favorable for hosting large spherical molecules such as $C_{60}(OH)_{20}$. Conceivably, such steric hindrance could be further reinforced by the prevalent binding of $C_{60}(OH)_{20}$ on the tubulin. Furthermore, the number of GTP molecules in the reaction buffer was 2 to 3 orders of magnitude higher than that of $C_{60}(OH)_{20}$ in the experiment, implying that it was far more likely for $C_{60}(OH)_{20}$ to bind to the free GTP/GDP molecules in the buffer than with the bound nucleotides in the tubulin.

Additional new insight has been obtained from the simulations. First, a tubulin dimer makes a number of contacts with its neighboring dimers when inserted into a MT. If $C_{60}(OH)_{20}$ molecules bind to these contact regions as indicated by docking and MD simulations, they can also prevent the incorporation of the dimer into a MT. The crystal structure of tubulin is obtained from zinc sheets in which the protofilaments are arranged similar to that in a MT, but the protofilaments are antiparallel in zinc sheets.[43] Thus, the longitudinal contacts seen in zinc sheets[26] are the same as that in a MT, but the lateral contacts could be different. Figure 9 shows a tubulin dimer with its longitudinal neighbors. The locations of the $C_{60}(OH)_{20}$ molecules that bind at these contact regions in MD simulations are also shown. It is possible that the binding of nanoparticles at these sites could impede MT polymerization or

cause MT aggregation, as indicated in Figure 1B. Second, in MD simulations, $C_{60}(OH)_{20}$ was also seen to bind the M-loop and H5 and H12 helices (Figure 10). The interaction between the M-loop in one dimer and helices in a neighboring dimer is a major contributor to lateral contacts between tubulin dimers in zinc sheets. Although the lateral contacts in MTs do not necessarily have to be the same as that in zinc sheets, the M-loop is involved in lateral contact in MTs. Thus $C_{60}(OH)_{20}$ could also affect the lateral contacts and thus MT assembly if bound to these motifs.

CONCLUSIONS

Our experimental and computer simulation studies have shown that $C_{60}(OH)_{20}$ can inhibit MT polymerization, mainly through the formation of hydrogen bonding between the nanoparticle and the tubulin dimer. The binding of the fullerene derivative has been shown experimentally to alter the secondary structures of the tubulin and impede the release of inorganic phosphate in GTP hydrolysis. Additional simulations have unravelled occupancy of the contacts between adjacent tubulin dimers within a protofilament and between neighboring tubulins by the nanoparticles, which should conceivably also influence the assembly of tubulins into MTs. Since MTs are important organelles whose structure and dynamics are essential to many functionalities and activities of the cell, this study facilitates our understanding of the biological response to engineered nanoparticles on the molecular level.

EXPERIMENTAL AND COMPUTATIONAL METHODS

MT Polymerization. Taxol-stabilized fluorescent MTs were polymerized using a Fluorescent Microtubules Biochem Kit (#BK007R, Cytoskeleton). Specifically, MT polymerization reactions (3 μL) were prepared, each consisting of 2.5 μL of unlabeled tubulin (#TL238, Cytoskeleton, 0.045 mM) and 0.5 μL of rhodamine-labeled tubulin (#TL331M, Cytoskeleton, 0.11 mM) suspended in the general tubulin buffer (or PEM buffer) (80 mM Na-PIPES pH 6.9, 1 mM $MgCl_2$, and 1 mM EGTA; #BST01, Cytoskeleton) to form a stock solution of one dye per three tubulin subunits (MW: 110 kDa). The general tubulin buffer also contained 0.03 μL of 100 mM GTP (#BST06, Cytoskeleton) for tubulin assembly. Prior to polymerization, fullerene derivative $C_{60}(OH)_{20}$ (BuckyUSA) was suspended in Milli-Q water (pH 6.5) to form a stock concentration of 100 mg/L, filtered, and sterilized using Anotop 10 filters (0.2 μm, Whatman). Approximately 0.5 μL of $C_{60}(OH)_{20}$ (6.6−198 μM) was added to 3 μL of MT polymerization reactions to obtain final $C_{60}(OH)_{20}$ concentrations of 1−30 mg/L (or 0.94−28.2 μM), respectively, and the mixtures were incubated at 35 °C for 20 min. Small aliquots of the polymerized MTs, each added with 1× antifade solution (#BSM02, Cytoskeleton), were examined by fluorescence microscopy (Imager A1, Zeiss), and approximately 200 MTs were measured for each sample condition to establish sufficient statistical distributions. Statistically significant differences between the samples and the controls were determined by the Student *t* test.

Characterization of $C_{60}(OH)_{20}$ Suspension. The hydrodynamic size of $C_{60}(OH)_{20}$ was measured at room temperature using a dynamic light scattering device (Malvern, nanosizer S90, range: 0.3 nm to 5 μm). Single peaks at ~1.0 nm (polydispersity index: 0.141) and 5.7 nm (polydispersity index: 0.443) were identified for the nanoparticles in Milli-Q water and in the PEM buffer. The stability of the $C_{60}(OH)_{20}$ suspension was further confirmed by its negative zeta potential of −34.3 mV in Milli-Q water and −22.0 mV in the PEM buffer. Such changes in the physicochemistry (size, polydispersity, and charge) of the nanoparticles are attributed to the presence of Na^+ and Mg^{2+} in the PEM buffer.

Circular Dichroism Spectroscopy. To probe the conformational change in the tubulin secondary structures due to $C_{60}(OH)_{20}$ binding, circular dichroism spectroscopy measurements were performed at room temperature using a Jasco J-810 spectropolarimeter (Easton, MD) with a constant temperature water-circulating bath over the wavelength range 200−300 nm. The structural contents of the tubulins were measured using 0.25 mg/mL tubulin solutions in Milli-Q water loaded into 0.10 mm path length high-transparency quartz cuvettes (Starna Cells, Inc., Atascadero, CA). Milli-Q water was used as the buffer due to the high transparencies of the samples. To prevent possible protein denaturation in the absence of salt, an obervation time of 1 h or less was ensured. The spectrum of each sample was averaged over three scans taken at a speed of 50 nm/min and subtracted by the blanks of Milli-Q water. The ellipticity value (θ, in mdeg) provided by the instrument was converted to standard units of deg·cm^2/dmol (designated as $[\theta]$) using the equation $[\theta] = (\theta \times M_0)/(10\,000 \times C_{soln} \times L)$,[23,24] where M_0 is the mean residue molecular weight (118 g/mol), C_{soln} is the tubulin concentration in solution (g/mL), and L is the path length through the buffer (cm).

The molar ellipticities as a function of wavelength that were obtained from the CD scans were deconvoluted using the SP-22X algorithm and analyzed using the SELCON and CONTIN/LL software[25] packages. Such deconvolution yielded the percents of secondary structure components (α helices and β sheets) in the protein samples. These programs analyze the ellipticity values at each wavelength and compare them with a library of proteins with known secondary structures. The percents of various secondary structural components are then derived on the basis of the comparisons.

Isothermal Titration Calorimetry. To provide detailed information on the binding of $C_{60}(OH)_{20}$ with tubulin, ITC measurements were performed on a VP-ITC microcalorimeter (MicroCal Inc., Northampton, MA). Tubulins were dialyzed extensively against PEM buffer without GTP to avoid microtubule polymerization, to a final concentration of 0.7 μM. The syringe content was 0.2 mM $C_{60}(OH)_{20}$ dissolved in the last dializant.

A typical titration involved 22 injections of $C_{60}(OH)_{20}$ (14 μL aliquots per shot) into the sample cell at a 4 min interval, each containing 1.46 mL of tubulin. The titration cell was kept at 298 K and stirred continuously at 300 rpm. The heat of diluting $C_{60}(OH)_{20}$ in the buffer alone was subtracted from the titration data when the thermodynamics parameters were calculated. All the data were analyzed to determine binding stoichiometry (N), affinity constants (K), and thermodynamic parameters of the reaction, using Origin 5.0 software.

GTP Hydrolysis. To detect the release of inorganic phosphate during the GTP hydrolysis that is associated with MT polymerization, a SensoLyte MG phosphate assay kit (AnaSpec) was used. This kit is based on the quantification of the blue-green complexes formed by Malachite Green, molybdates, and free orthophosphates, which are released during MT polymerization. The rapid color formation from the reaction was measured on an absorbance microplate reader at 630 nm (μQuant, BioTek Instuments, Inc.).

Computational Methods. Two computational methods, namely, molecular docking and molecular dynamics (MD), were used to find out (i) the possible binding sites of $C_{60}(OH)_{20}$ on tubulin α−β dimer and (ii) how the binding of $C_{60}(OH)_{20}$ affects the structure and dynamics of the tubulin dimer. The molecular structure of the dimer was obtained from protein data bank (PDB ID: 1JFF[26]). The missing residues in the PDB structure were added using MODELER 9v7,[27] and the complete dimer was energy minimized using a steepest descent algorithm.

Docking Simulation. Molecular docking is a computational method used to assess the binding modes and affinities of small molecules (*e.g.*, drugs) on larger molecules such as proteins. Here, docking of $C_{60}(OH)_{20}$ was carried out on tubulin to predict the possible binding sites and binding affinities. One of the most popular docking software packages, AutoDock[28] (version 4.2), was used. The PDB structure may not represent the actual protein structure, which constantly undergoes conformational changes due to thermal motion. For a more realistic approach, docking can be performed on conformations obtained from MD simulations. Here we performed docking calculations on the conformation at 10 ns of the MD simulation in addition to the PDB structure. Default AutoDock force field parameters[29] were used, setting all bonds rigid except the C−O bonds of $C_{60}(OH)_{20}$, which were made rotatable. Fifty docking runs with 10 trials in each run were performed for both dimer conformations, resulting in a total of 1000 docked structures.

MD Simulation. The binding of $C_{60}(OH)_{20}$ may affect the secondary, tertiary, and quaternary structures of tubulin dimers and hence their polymerization into MTs. Since MD simulations are capable of capturing such structural changes, two sets of simulations were carried out to examine this aspect. In the first set (referred to as *set I* in the following) a tubulin dimer was simulated with GTP and guanosine diphosphate (GDP) bound to it as in the PDB crystal structure (PDB ID: 1JFF). In the other set (*set II*), the dimer−GTP−GDP complex was simulated with 10 $C_{60}(OH)_{20}$ molecules placed randomly around it. In both sets, the protein complex (with or without $C_{60}(OH)_{20}$ as the case may be) was placed at the center of the simulation box. The size of the box in each case was decided so that the distance from the protein complex (or $C_{60}(OH)_{20}$) to any edge of the box was at least 0.9 nm. The number of water molecules added was approximately 40 000. Thirty-six Na^+ ions were added for charge neutrality. In addition, 122 Na^+ and Cl^- ions were also added such that the salt concentration in the simulation box was about 100 mM. Each of these steps was followed by energy minimization using a steepest descent algorithm, as implemented in GROMACS 4.5.[30]

Four independent simulations were carried out for each set. Each simulation was initiated with a 50 ps long *NVT* thermalization run, followed by a 100 ps long *NPT* simulation, during which the protein/GTP/GDP/$C_{60}(OH)_{20}$ heavy atoms were position restrained. Finally, a 50 ns long unrestrained production run was carried out at $T = 298$ K and $P = 1$ bar.

The simulations were carried out with the GROMACS simulation package, version 4.5.[30] The Gromos 53A6 force field[31] was used with the SPC model for water.[32] The parameters for GTP and GDP were obtained by augmenting the guanine model of Gromos 53A6 with the triphosphate side chain parameters of ATP in the same force field.[31] For charge states of −4 and −3 for GTP and GDP, respectively, the terminating phosphate group charges were set as in our previous study with dGTP.[18] The model for $C_{60}(OH)_{20}$ was adapted from ref 18.

The LINCS algorithm[33] was used to restrain all the bonds, and an integration time step of 2 fs was used. Long-range electrostatics was treated with the particle-mesh Ewald[34] method. In all the simulations, the system temperature was maintained at 298 K by using the velocity rescaling algorithm by Bussi *et al.*[35] The system pressure was controlled by using the weak coupling algorithm by Berendsen *et al.*,[36] with a coupling time constant $\tau_T = 0.5$ ps in the restrained *NPT* simulations, and the Parrinello−Rahman barostat[37,38] ($\tau_T = 2.0$ ps) in the unrestrained production runs.

Acknowledgment. This work was supported by an NSF CAREER award CBET-0744040 to P.C.K. and the Academy of Finland general research grant #127091 to E.S. The authors thank Dr. Dev Arya for the use of a MicroCal VP-ITC system and Pengyu Chen for assistance with data analysis.

REFERENCES AND NOTES

1. Colvin, V. L. The Potential Environmental Impact of Engineered Nanomaterials. *Nat. Biotechnol.* **2003**, *21*, 1166–1170.
2. Nel, A.; Xia, T.; Madler, L.; Li, N. Toxic Potential of Materials at the Nanolevel. *Science* **2006**, *311*, 622–627.
3. Maynard, A. D.; Aitken, R. J.; Butz, T.; Colvin, V. L.; Donaldson, K.; Oberdörster, G.; Philbert, M. A.; Ryan, J.; Seaton, A.; Stone, V.; *et al.* Safe Handling of Nanotechnology. *Nature* **2006**, *444*, 267–269.
4. Ke, P. C.; Qiao, R. Carbon Nanomaterials in Biological Systems. *J. Phys.: Condens. Matter* **2007**, *19*, 373101-1–25.
5. Friedman, S. H.; DeCamp, D. L.; Sijbesma, R. P.; Srdanov, G.; Wudl, F.; Kenyon, G. L. Inhibition of the HIV-1 Protease by Fullerene Derivatives: Model Building Studies and Experimental Verification. *J. Am. Chem. Soc.* **1993**, *115*, 6506–6509.
6. Zhu, J.; Ji, Z.; Wang, J.; Sun, R.; Zhang, X.; Gao, Y.; Sun, H.; Liu, Y.; Wang, Z.; Li, A.; *et al.* Tumor-Inhibitory Effect and Immunomodulatory Activity of Fullerol $C_{60}(OH)_x$. *Small* **2008**, *4*, 1168–1175.
7. Ashcroft, J. M.; Tsyboulaski, D. A.; Hartman, K. B.; Zakharian, T. Y.; Marks, J. W.; Weisman, R. B.; Rosenblum, M. G.; Wilson, L. J. Fullerene (C_{60}) Immunoconjugates: Interaction of Water-Soluble C_{60} Derivatives with the Murine Anti-gp240 Melanoma Antibody. *Chem. Commun.* **2006**, 3004–3006.
8. Hwang, K. C.; Mauzerall, D. Photoinduced Electron Transport across a Lipid Bilayer Mediated by C_{70}. *Nature* **1993**, *361*, 138–140.
9. Chen, R.; Ratnikova, T. A.; Stone, M. B.; Lin, S.; Lard, M.; Huang, G.; Hudson, J. S.; Ke, P. C. Differential Uptake of Carbon Nanoparticles by Plant and Mammalian Cells. *Small* **2010**, *6*, 612–617.
10. Oberdorster, E. Manufactured Nanomaterials (Fullerenes, C_{60}) Induce Oxidative Stress in the Brain of Juvenile Largemouth Bass. *Environ. Health Perspect.* **2004**, *112*, 1058–1062.
11. Sayes, C. M.; Fortner, J. D.; Guo, W.; Lyon, D.; Boyd, A. M.; Ausman, K. D.; Tao, Y. J.; Sitharaman, B.; Wilson, L. J.; Hughes, J. B.; *et al.* The Differential Cytotoxicity of Water-Soluble Fullerenes. *Nano Lett.* **2004**, *4*, 1881–1887.
12. Qiao, R.; Roberts, A. P.; Mount, A. S.; Klaine, S. J.; Ke, P. C. Translocation of C_{60} and Its Derivatives across a Lipid Bilayer. *Nano Lett.* **2007**, *7*, 614–619.
13. Wong-ekkabut, J.; Baoukina, S.; Triampo, W.; Tang, I. M.; Tieleman, D. P.; Monticelli, L. Computer Simulation Study of Fullerene Translocation through Lipid Membranes. *Nat. Nanotechnol.* **2008**, *3*, 363–368.
14. Salonen, E.; Lin, S.; Reid, M. L.; Allegood, M. S.; Wang, X.; Rao, A. M.; Vattulainen, I.; Ke, P. C. Real-Time Translocation of Fullerene Reveals Cell Contraction. *Small* **2008**, *4*, 1986–1992.
15. Gharbi, N.; Pressac, M.; Hadchouel, M.; Szwarc, H.; Wilson, S. R.; Moussa, F. [60]Fullerene is a Powerful Antioxidant in Vivo with No Acute or Subacute Toxicity. *Nano Lett.* **2005**, *5*, 2578–2585.
16. Song, G.; Yao, L.; Huang, C.; Xie, X.; Yang, X. Inhibition of DNA Restrictive Endonucleases by Aqueous Nanoparticle Suspension of Methanophosphonate Fullerene Derivatives and Its Mechanisms. *Sci. China Ser. B: Chem.* **2009**, *52*, 626–631.
17. Meng, X; Li, B.; Chen, Z.; Yaw, L.; Zhao, D.; Yang, X.; He, M.; Yu, Q. Inhibition of A Thermophilic Deoxyribonucleic Acid Polymerase by Fullerene Derivatives. *J. Enzyme Inhib. Med. Chem.* **2007**, *22*, 293–296.
18. Shang, J.; Ratnikova, T. A.; Anttalainen, S.; Salonen, E.; Ke, P. C.; Knap, H. Experimental and Simulation Studies of Real-Time Polymerase Chain Reaction in the Presence of a Fullerene Derivative. *Nanotechnology* **2009**, *20*, 415101–1−8.
19. Lin, S.; Reppert, J.; Hu, Q.; Hudson, J. S.; Reid, M. L.; Ratnikova, T. A.; Rao, A. M.; Luo, H.; Ke, P. C. Uptake, Translocation and Transmission of Carbon Nanomaterials in Rice Plants. *Small* **2009**, *5*, 1128–1132.
20. Gheshlaghi, Z. N.; Riazi, G. H.; Ahmadian, S.; Ghafari, M.; Mahinpour, R. Toxicity and Interaction of Titanium Dioxide Nanoparticles with Microtubule Protein. *Acta Biochim. Biophys. Sin.* **2008**, *40*, 777–782.

21. Apopa, P. L.; Qian, Y.; Shao, R.; Guo, N. L.; Schwegler-Berry, D.; Pacurari, M.; Porter, D.; Shi, X.; Vallyathan, V.; Castranova, V.; *et al.* Iron Oxide Nanoparticles Induce Human Microvascular Endothelial Cell Permeability through Reactive Oxygen Species Production and Microtubule Remodeling. *Part. Fibre Toxicol.* **2009**, *6*, 1–14.
22. Zhou, J. C.; Wang, X.; Xue, M.; Xu, Z.; Hamasaki, T.; Yang, Y.; Wang, K.; Dunn, B. Characterization of Gold Nanoparticle Binding to Microtubule Filaments. *Mater. Sci. Eng., C* **2010**, *30*, 20–26.
23. Greenfield, N. J. Using Circular Dichroism Collected as a Function of Temperature to Determine the Thermodynamics of Protein Unfolding and Binding Interactions. *Nat. Protoc.* **2006**, *1*, 2527–2535.
24. Sreerama, N.; Woody, R. W. Computation and Analysis of Protein Circular Dichroism Spectra. *Methods Enzymol.* **2004**, *383*, 318–351.
25. Sreerama, N.; Woody, R. W. Estimation of Protein Secondary Structure from Circular Dichroism Spectra: Comparison of CONTIN, SELCON, and CDSSTR Methods with an Expanded Reference Set. *Anal. Biochem.* **2000**, *287*, 252–260.
26. Lowe, J.; Li, H.; Downing, K. H.; Nogales, E. Refined Structure of $\alpha\beta$ Tubulin at 3.5 Å Resolution. *J. Mol. Biol.* **2001**, *313*, 1045–1057.
27. Fiser, A.; Do, R. K. G.; Sali, A. Modeling of Loops in Protein Structures. *Protein Sci.* **2000**, *9*, 1753–1773.
28. Morris, G. M.; Huey, R.; Lindstrom, W.; Sanner, M. F.; Belew, R. K.; Goodsell, D. S.; Olson, A. J. AutoDock4 and AutoDockTools4: Automated Docking with Selective Receptor Flexibility. *J. Comput. Chem.* **2009**, *30*, 2785–2791.
29. Huey, R.; Morris, G. M.; Olson, A. J.; Goodsell, D. S. A Semiempirical Free Energy Force Field with Charge-Based Desolvation. *J. Comput. Chem.* **2006**, *28*, 1145–1152.
30. Hess, B.; Kutzner, C.; van der Spoel, D.; Lindahl, E. Gromacs 4: Algorithms for Highly Efficient, Load-Balanced, and Scalable Molecular Simulation. *J. Chem. Theory Comput.* **2008**, *4*, 435–447.
31. Oostenbrink, C.; Villa, A.; Mark, A. E.; van Gunsteren, W. F. A Biomolecular Force Field Based on the Free Enthalpy of Hydration and Solvation: The GROMOS Force-Field Parameter Sets 53A5 and 53A6. *J. Comput. Chem.* **2004**, *25*, 1656–1676.
32. Berendsen, H. J. C.; Postma, J. P. M.; van Gunsteren, W. F.; Hermans, J. *Intermolecular Forces*; Pullman, B., Ed.; Reidel: Dordrecht, 1981; pp 331−334.
33. Hess, B.; Bekker, H.; Berendsen, H. J. C.; Fraaije, J. G. E. M. LINCS: A Linear Constraint Solver for Molecular Simulations. *J. Comput. Chem.* **1997**, *18*, 1463–1472.
34. Essmann, U.; Perera, L.; Berkowitz, M. L.; Darden, T.; Lee, H.; Pedersen, L. G. A Smooth Particle Mesh Ewald Potential. *J. Chem. Phys.* **1995**, *103*, 8577–8592.
35. Bussi, G.; Donadio, D.; Parrinello, M. Canonical Sampling through Velocity Rescaling. *J. Chem. Phys.* **2007**, *126*, 014101-1–7.
36. Berendsen, H. J. C.; Postma, J. P. M.; van Gunsteren, W. F.; DiNola, A.; Haak, J. R. Molecular Dynamics with Coupling to An External Bath. *J. Chem. Phys.* **1984**, *81*, 3684–3690.
37. Parrinello, M.; Rahman, A. Polymorphic Transitions in Single Crystals: A New Molecular Dynamics Method. *J. Appl. Phys.* **1981**, *52*, 7182–7190.
38. Nose, S.; Klein, M. L. Constant Pressure Molecular Dynamics for Molecular Systems. *Mol. Phys.* **1983**, *50*, 1055–1076.
39. Howard, J.; Hyman, A. A. Growth, Fluctuation and Switching at Microtubule Plus Ends. *Nat. Rev.* **2009**, *10*, 569–574.
40. Nogales, E.; Wang, H.-W. Structural Intermediates in Microtubule Assembly and Disassembly: How and Why? *Curr. Opin. Cell Biol.* **2006**, *18*, 179–184.
41. Kabsch, W.; Sander, C. Dictionary of Protein Secondary Structure: Pattern Recognition of Hydrogen-Bonded and Geometrical Features. *Biopolymers* **1983**, *22*, 2577–2637.
42. Matthes, D.; de Groot, B. L. Secondary Structure Propensity in Protein Folding Simulations: A Systematic Comparison of Molecular Mechanics Interaction Schemes. *Biophys. J.* **2009**, 599–608.
43. Crepeau, R. H.; McEwen, B.; Edelstein, S. J. Differences in α and β Polypeptide Chains of Tubulin Resolved by Electron Microscopy with Image Reconstruction. *Proc. Natl. Acad. Sci.* **1978**, *75*, 5006–5010.